AGU ADVANCING EARTH AND SPACE SCIENCE

Geophysical Research Letters®

RESEARCH LETTER
10.1029/2021GL095065

Magnetospheric Multiscale Observations of an Expanding Oxygen Wave in Magnetic Reconnection

Håkon Midthun Kolstø[1], Cecilia Norgren[1], Michael Hesse[2], Li-Jen Chen[3], Paul Tenfjord[1], Susanne Flø Spinnangr[1], and Norah Kwagala[1]

[1]Space Plasma Physics Group, University of Bergen, Bergen, Norway, [2]NASA Ames Research Center, Mountain View, CA, USA, [3]NASA Goddard Space Flight Center, Greenbelt, MD, USA

Key Points:

- Observation of Hall electric field accelerated O^+ inside separatrix density cavity
- Observational evidence of predicted oxygen wave
- Observed oxygen dynamics and corresponding velocity distribution functions consistent with simulation predictions

Correspondence to:
H. M. Kolstø,
hakon.kolsto@uib.no

Citation:
Kolstø, H. M., Norgren, C., Hesse, M., Chen, L.-J., Tenfjord, P., Spinnangr, S. F., & Kwagala, N. (2021). Magnetospheric multiscale observations of an expanding oxygen wave in magnetic reconnection. *Geophysical Research Letters*, *48*, e2021GL095065. https://doi.org/10.1029/2021GL095065

Received 30 JUN 2021
Accepted 9 SEP 2021

Abstract Heavier plasma species such as oxygen ions can have a large impact on the magnetic reconnection process. It has been hypothesized that the acceleration of demagnetized oxygen ions by the Hall electric field will lead to the formation of an oxygen wave that expands into the exhaust. By comparing data from NASA's Magnetospheric Multiscale mission to a fully kinetic particle-in-cell simulation, we can for the first time provide observational evidence of such an expanding oxygen wave. The wave is characterized by an oxygen jet consisting of cold ions directed toward the neutral sheet associated with a density cavity. This density cavity forms as the O^+ are subject to collective acceleration by the Hall electric field leaving behind a region of low-density oxygen ions. Our results are important for the understanding of the role and effect of oxygen ions in magnetic reconnection.

Plain Language Summary Magnetic reconnection is one of the most important energy release and transport processes in plasmas. In the case of the Earth's magnetosphere, magnetic reconnection is the primary mechanism responsible for the transport of energy, mass, momentum, and magnetic flux into Earth's magnetic cavity. On the night side of Earth in a region called the magnetotail, magnetic flux is transported from the north and south to meet in a current layer that extends across the width of the magnetosphere. While the most common plasma species in the magnetotail are protons and electrons, during high geomagnetic activity heavier ion species, such as oxygen, can sometimes dominate during high geomagnetic activity. Using data collected by NASA's Magnetospheric Multiscale mission together with numerical simulation, we investigate how oxygen ions contribute to the reconnection process.

1. Introduction

Magnetic reconnection is one of the most important energy conversion and transport processes in space plasma. It converts stored magnetic energy to thermal and kinetic energy of the plasma species. In addition to protons and electrons, multispecies plasma is commonly observed by various spacecraft in our magnetosphere (Baker et al., 1982; Chappell et al., 1987; Moore et al., 2001). Oxygen ions present in the plasma sheet, originating from the high-latitude ionosphere have been widely reported (Frank et al., 2012; Grande et al., 2013; Moore et al., 2001; Mouikis et al., 2018; Toledo-Redondo et al., 2021; Wilken et al., 1995; Zong et al., 1998). The ionospheric outflow rate of these oxygen ions has been found to scale with geomagnetic activity (Baker et al., 1982) and the rate is significantly enhanced during storm time conditions. Spacecraft observations by Cluster reveal that O^+ may, at storm time, be the dominating ion species (Kistler et al., 2005; Wygant et al., 2005).

As the reconnection process converts electromagnetic energy to both thermal and kinetic energy of the plasma, the presence of O^+ in the reconnection region may strongly affect the energy partitioning. Compared to protons, the higher mass of the oxygen ions results in larger gyro radii at similar energies giving rise to multiscale diffusion regions where the O^+ becomes demagnetized (Liu et al., 2015). As reconnection proceeds, the demagnetization of O^+ introduces distinct spatial and temporal scales for the reconnection process (Liu et al., 2014, 2015; Shay & Swisdak, 2004). Tenfjord et al. (2019) showed that although oxygen ions are to a higher degree demagnetized, they can act as an energy sink, resulting in a reduction of the reconnection rate.

Cluster observations reported the existence of oxygen ions being ballistically accelerated by the Hall electric field, giving rise to counter streaming velocity distribution signatures (Wygant et al., 2005). Similar characteristics were also found in particle-in-cell simulations (Liang et al., 2017). Tenfjord et al. (2018) found that as the Hall electric field grows and expands further out in the lobes and downstream, oxygen ions are collectively accelerated giving rise to expanding oxygen jets. The front of these jets consists of propagating localized regions of high O^+ density which are referred to as oxygen waves (Tenfjord et al., 2018). This study provides the first observational evidence of such an expanding oxygen wave captured by NASA's Magnetospheric Multiscale (MMS) mission.

The paper is structured as follows: in Section 2, we introduce an overview of the MMS observations. In Section 3, we describe the simulation setup that is used to contextualize the observations. Section 4 examines the O^+ reconnection dynamics in the exhaust by comparing moments and velocity distribution functions (VDF) from both MMS and particle-in-cell simulations (PIC). This section further reports on the observational evidence of an expanding oxygen wave.

2. MMS Event Overview

The observational data used in this analysis has been collected by MMS. We present data from the Hot Plasma Composition Analyzer (HPCA) (Young et al., 2016), the Fluxgate Magnetometers (FGM) (Russell et al., 2016), the Fast Plasma Investigation (FPI) (Pollock et al., 2016), and the Electric field Double Probes (EDP) (Ergun et al., 2016; Lindqvist et al., 2016).

Figures 1a–1f show an overview of the event as observed by MMS1 on the fourth of August 2017 at [−21.5, 8.3, 2.6] Earth radii (R_e) in Geocentric Solar Magnetospheric (GSM) coordinates around 09:56–10:05 Universal Time (UT). As MMS1–4 all observe similar features, we only show data from one spacecraft. The minimum variance direction, N, represents the current sheet normal direction and is found through a Minimum Variance Analysis on the magnetic field (MVA-B) (Sonnerup & Cahill, 1967) between 09:41:30 and 10:02:30 UT. As seen in Figure 1a, $B_N = 0$ nT at the beginning of the time interval, but gradually increases to $B_N \sim 10$ nT at the end. This increase in B_N is not directly related to the exhaust signatures (i.e., B_N is finite even when MMS has exited the main jet) and, therefore, we believe this can be attributed to current sheet rotation or tilting at the time of the investigation. To complete our coordinate system, we choose $\vec{L}$ such that B_L is the dominant component of **B** at the beginning of the time interval. We note, however, the possibility of a finite guide field. The choice of $\vec{L}$ also roughly maximizes the outflow speeds v_L^e and ion v_L^i, which we expect in the reconnection outflow. Our final LMN-coordinate system is then given by $\vec{L} = (0.92, -0.31, -0.25)$, $\vec{M} = (0.09, 0.79, -0.61)$, and $\vec{N} = (0.39, 0.54, 0.75)$ (GSM), where L is the implied reconnection outflow direction, and M is the current direction.

Throughout the interval, $B_L > 0$. Since $\hat{L} \sim \hat{x}_{GSM}$, we conclude that the spacecraft remained north of the neutral sheet during the observed time interval. As the spacecraft moves toward the neutral sheet, MMS observes increasing B_M, which coincides with the strong E_N (Figure 1b). We identify E_N and B_M as the Hall electric and magnetic fields, respectively. Furthermore, we note the increasing value of E_M which, at later times, becomes proportional to E_N. This suggests that the N and M vectors are locally a nonperfect coordinate system, i.e., the current sheet normal direction is actually a mix of N and M.

Between 10:01 and 10:03 UT, strong Earthward ($v_L > 0$) ion and electron jets, reaching speeds up to 1,000 km/s, are observed by FPI (Figures 1c and 1d). The strong Hall fields and jets indicate that the spacecraft has entered the reconnection exhaust. The oxygen velocity $v_L^{O^+}$ (Figure 1e) is clearly decoupled from these high velocities, instead showing a consistent Earthward-flowing component of ~150–200 km/s. Whereas the FPI ion and electrons predominantly show Earthward-flowing bulk velocities, the oxygen ions experience strong flows toward the neutral sheet seen in Figure 1e at ~10:02 UT reaching values of $v_N^{O^+} \approx -500$ km/s. This region of enhanced negative $v_N^{O^+}$ coincides with a region of low O^+ density ($n_{O+} = 0.006\ \mathrm{cm}^{-3}$) (Figure 1f). This density cavity is bordered by two regions of slightly enhanced n_{O+} (labeled A and C) with values of 0.025 cm^{-3}. Inside the cavity, the drifting ion population approaches the energy cutoff of the HPCA instrument. When the high-speed flow is observed, the drifting component is resolved. However, during the first part of the cavity at ~10:01:30–10:02:00 UT, it is possible that the beam has exceeded the HPCA energy limit. The O^+ density should therefore be considered as a lower limit.

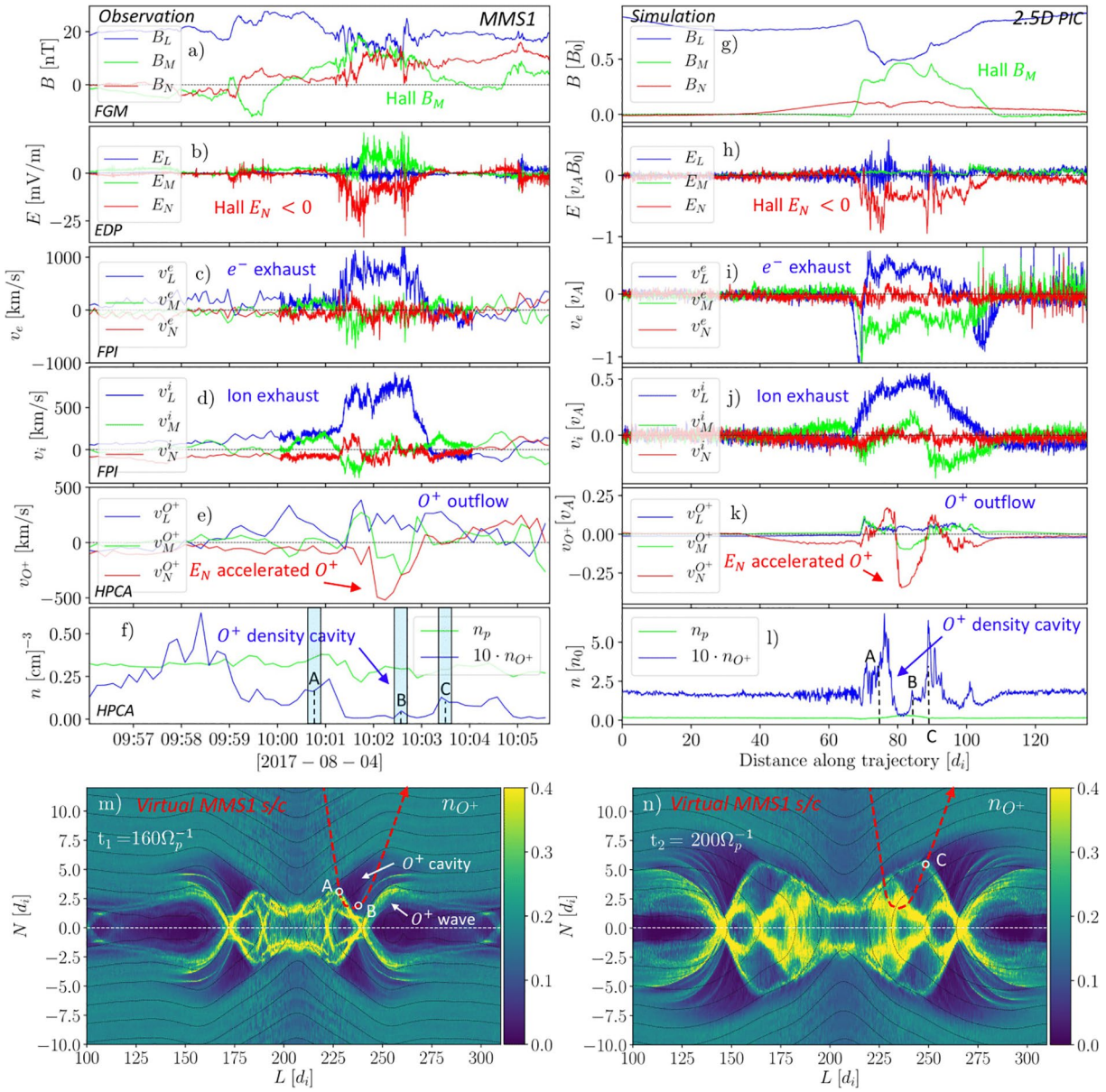

Figure 1. (a–f) Observational data collected by the MMS1 spacecraft. (a) Magnetic field, (b) electric field, (c) FPI electron, and (d) ion bulk velocities. (e) HPCA O^+ bulk velocity. (f) HPCA O^+ and H^+ density. Burst data are collected between 10:00:04 and 10:04:56. (g–l) Simulation data collected by a virtual spacecraft whose trajectory is overlaid on the O^+ density depicted in the color map (m, n) at times t_1 and t_2 (g) Magnetic field and (h) electric field. (i) Electron and (j) proton bulk velocities. (k) O^+ bulk velocity. (l) O^+ and H^+ density. Points marked A, B, and C, in panels (f, l, m, and n) correspond to the location where the VDFs have been extracted. The shaded area in (f) corresponds to the collection time (~10 s) to calculate the VDFs. The relative motion traced in (m, n) is attributed to the N-directed flapping of the current sheet together with the tailward motion of the reconnection site.

There is also a clear enhancement of $n_{O+} \approx 0.055\text{cm}^{-3}$ around 09:58 UT, prior to the encounter of the exhaust jet. The origin of this enhancement is unknown but may be due to variations in the inflow regions. However, in this paper, we seek to understand the origin of the O^+ density structures and dynamics observed in the reconnection exhaust. In order to gain deeper insight into the structures observed by MMS, we utilize a 2.5D PIC simulation.

3. Simulation Setup

The magnetic field configuration is given by a generalized Harris-type equilibrium defined as $B_x = B_0 \tanh(z/\lambda)$, where $\lambda = 2d_p$ is the half width of the initial current sheet, and $d_p = c/\omega_{pi} (= c\sqrt{\epsilon_0 m_p/n_0 e^2})$ is the proton inertial length (see Hesse et al., 1999 for details). Densities are normalized to the foreground density at the center of the initial current sheet n_0, lengths to d_p, and time to the inverse of the proton cyclotron frequency $\Omega_p^{-1} = m_p/eB_0$. A uniform proton density distribution of $n_b = 0.2$ is added to the initial Harris-sheet density configuration $n_p = n_0/\cosh^2(z/\lambda)$ resulting in a peak density of 1.2 in the current layer. Oxygen ions are homogeneously distributed above a specific field line, corresponding to a distance of $|z| > 3d_p$ from the current sheet with $n_{O^+} = 0.2$. The O^+ has initially zero thermal velocity. The mass ratios are: $n_p/m_e = 25$ for the protons/electrons and $m_{O^+}/m_p = 16$ for the oxygen/protons. A total of $\sim 10^{10}$ macroparticles are used. Boundary conditions are periodic at $x = x_{min}$ and $x = x_{max}$. At $z = z_{min}$ and $z = z_{max}$, specular reflection is enabled and the out-of-plane electric field E_y is set to zero, preserving magnetic flux in the simulation domain. The size of our simulation domain is $410d_p \times 50d_p$ with a grid size of $6,400 \times 1,600$. We employ a time step of $\omega_{pe}\delta t = 0.5$. The velocity normalization is the proton Alfvén speed, based on the foreground current sheet density n_0. The foreground temperatures fulfill $T_p + T_e = 0.5$, in units of $[m_p v_A^2]$, derived from pressure balance $n_0(T_p + T_e) = B_0^2/2$. The ratio of the proton-electron temperature is $T_p/T_e = 5$. The ratio between the electron plasma frequency and gyrofrequency is $\omega_{pe}/\Omega_e = 2$. Based on the observed conditions from Figures 1a and 1f ($B = 24$ nT and $n = 0.35\,\mathrm{cm}^{-3}$), we infer the Alfvén velocity and ion inertial length to be $v_A \approx 920$ km/s and $d_i \approx 396$ km, respectively. The simulation used in this study was not designed to represent this exact event, but rather, a general reconnection process with high abundance O^+ made to capture the additional effects introduced by heavier plasma species.

4. O^+ Reconnection Dynamics; MMS and PIC Comparison

Based on the data collected by MMS, Figure 1, we utilize the PIC simulation to search for a simple virtual spacecraft trajectory that enables us to contextualize the observations. This further aids in understanding the O^+ dynamics and density structure seen in Figures 1e and 1f, respectively. In Figures 1g–1l, we see the observables extracted from a possible trajectory overlaid in the O^+ density map in Figures 1m and 1n.

The trajectory is constructed by first matching the $\mathbf{B}_{FGM}$ and $\mathbf{B}_{PIC}$ data, providing us with an indication of the location of MMS with respect to the neutral sheet. Note that this simple trajectory captures the additional signatures encountered by MMS such as E_N and the FPI ion and electron bulk velocities $\mathbf{v}^i_{LMN}$, $\mathbf{v}^e_{LMN}$. Upon entering the reconnection exhaust, the virtual spacecraft first encounters a region of enhanced n_{O^+} (labeled A) before dropping into a region of low n_{O^+}. This region of low n_{O^+} is identified as the O^+ density cavity (seen in Figures 1l and 1m). From Figure 1k, we also see the sudden increase of $-v_N^{O^+}$ in direct correspondence with the O^+ density cavity. We note that the density cavity observed by MMS is slightly broader than the jet structure, which is not the case for the simulation. This may be due to beam thermalization or trapping that reduces the bulk speed but conserves the density. Additionally, at the earlier edge of the cavity, where $|v_N|$ peaks, the beam approaches the highest energy levels of HPCA. We therefore also speculate that the beam may be broader than observed, but that this part of the beam is outside the energy range of HPCA.

We note that the oxygen density in the simulation exceeds that in the observations by a large margin. This is due to the initial conditions of the simulation, where the inflow oxygen density was relatively high. However, while the impact of the oxygen on the reconnection process would be affected by these relatively large differences in density, the demagnetized behavior of the oxygen in the outflow regions is qualitatively the same.

As seen in Figure 1f, MMS crossed the n_{O^+} density enhancement (labeled C) before exiting the reconnection region, thus marking the edge of the density cavity and the region of strong v_N-flows. In the simulation overview in Figures 1m, there are no signatures of a clear second density enhancement (as detected in the HPCA n_{O^+}, see label C in Figure 1f) along the trajectory after the cavity. The total time spent between the first (A) and the second (B) density enhancements in the observation is $\Delta t \sim 140\text{s} \approx 325\Omega_p^{-1}$ ($B = 24$ nT). During this time, the O^+ density structures may have experienced a significant expansion, thus we cannot

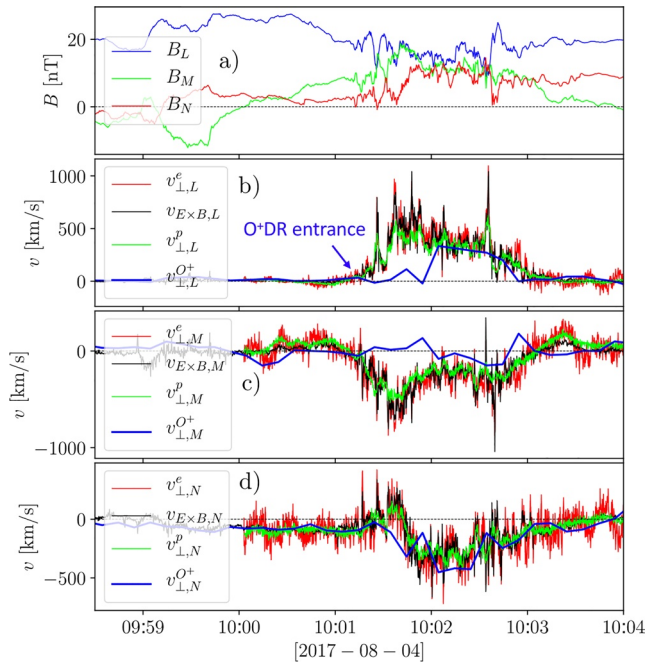

Figure 2. Comparison between $\mathbf{v}_{E\times B}$ and perpendicular velocities of ions (FPI), electrons (FPI), and oxygen (HPCA). (a) Magnetic field. (b–d) The components of the perpendicular velocities and $v_{E\times B}$. At ~10:01 UT, we see clear signs of demagnetization of oxygen ions marking the entrance of the O^+ diffusion region.

expect the simple quasi-stationary case. Therefore, we propose the following scenario; MMS enters the reconnection site and passes the density enhancement to enter the cavity. During the time Δt, the O^+ density structures expand, and as MMS exits the reconnection region it encounters the expanded structure at a different location in space and time. To probe this proposed scenario, a spatiotemporal trajectory is utilized to account for the time evolution of the density structures. Between points A and C, we let the simulation evolve in time allowing the O^+ front to expand such that the density structure again catches up to the spacecraft.

The remarkable similarities between the data observed by MMS and the data along our virtual trajectory strongly suggest that MMS passes through a region similar to that observed in the simulations. We thus hypothesize that the O^+ density cavity, seen in Figure 1f, is similar to the cavity in the simulation (Figures 1l) which forms due to the collective acceleration by E_N resulting in an oxygen wavefront propagating in the negative N-direction. In Sections 4.1 and 4.2, we examine whether the O^+ in the observations exhibit the demagnetized properties needed to give rise to such density signatures.

4.1. Dynamics of O^+ in the Reconnection Exhaust

The observed low-density region of O^+, referred to as the oxygen density *cavity* (see Figure 1f at 10:02 UT), originates from the demagnetized behavior of the oxygen ions. As reconnection proceeds, the Hall electric field expands due to the increasingly decoupled motion of the ions and electrons. If the oxygen ions are demagnetized, their initial motion while entering the reconnection exhaust will predominantly be due to E_N (Tenfjord et al., 2018). Due to the growth and expansion of E_N, the O^+ situated in the lobes will be picked up by the Hall electric field and accelerated toward the neutral line forming a propagating O^+ density front, i.e., the oxygen wave. In the simulation domain depicted in Figures 1m and 1n, we see an example of an oxygen wave by the slanted regions of high density that expand. As a large region of oxygen ions experience a strong acceleration by the expanding E_N, a wake of low O^+ density arises, resulting in a density cavity. These signatures are seen in Figures 1m and 1n as darker regions, indicating the absence of oxygen ions, followed by the intensified bands of high abundance O^+ density striations. These structures have previously been discussed by Tenfjord et al. (2018) and Kolstø et al. (2020b). The oxygen ions studied in this simulation reveal a demagnetized behavior as the oxygen cyclotron period is significantly longer than the characteristic time evolution of the reconnection process ($\sim\Omega_p^{-1}$). To investigate the degree of demagnetization of the observed O^+, we compare $\vec{v}_{E\times B} = \vec{E}\times\vec{B}/B^2$ to $\vec{v}_\perp$ of electrons and ions as measured by FPI (predominantly protons), and oxygen as measured by HPCA. This comparison is seen in Figures 2b–2d. In Figure 2a, we show **B** for context. In the lobe, all species follow $\vec{v}_{E\times B}$ closely. The encounter of the ion and electron jets at ~10:01 UT corresponds to MMS's entrance into the reconnection region. At this time, we begin to see the deviation of $\vec{v}_\perp^{O^+}$ from $\vec{v}_{E\times B}$, demonstrating a multiscale diffusion region nature, and the demagnetization of O^+. Inside this O^+ diffusion region, $v_{\perp,L}^{O^+}$ and $v_{\perp,M}^{O^+}$ deviate significantly (by approximately 500 km/s) from $v_{E\times B}$. Meanwhile, the deviation is slightly smaller for the normal component with approximately 250 km/s at ~10:01:30 UT. Overall we conclude that the deviation within the exhaust is significant for the demagnetization of the oxygen ions. Throughout the time of investigation, the protons as measured by FPI remained magnetized, indicating that MMS never entered the proton, much less the electron, diffusion regions.

In Section 4.2, we compare PIC and HPCA O^+ VDFs to gain an understanding of the behavior of the oxygen ions within the reconnection exhaust. Further, we investigate if the observed density enhancements, representing the edges of the cavity (Figure 1f), are consistent with the density enhancements encountered by the proposed simulation trajectory (Figure 1l).

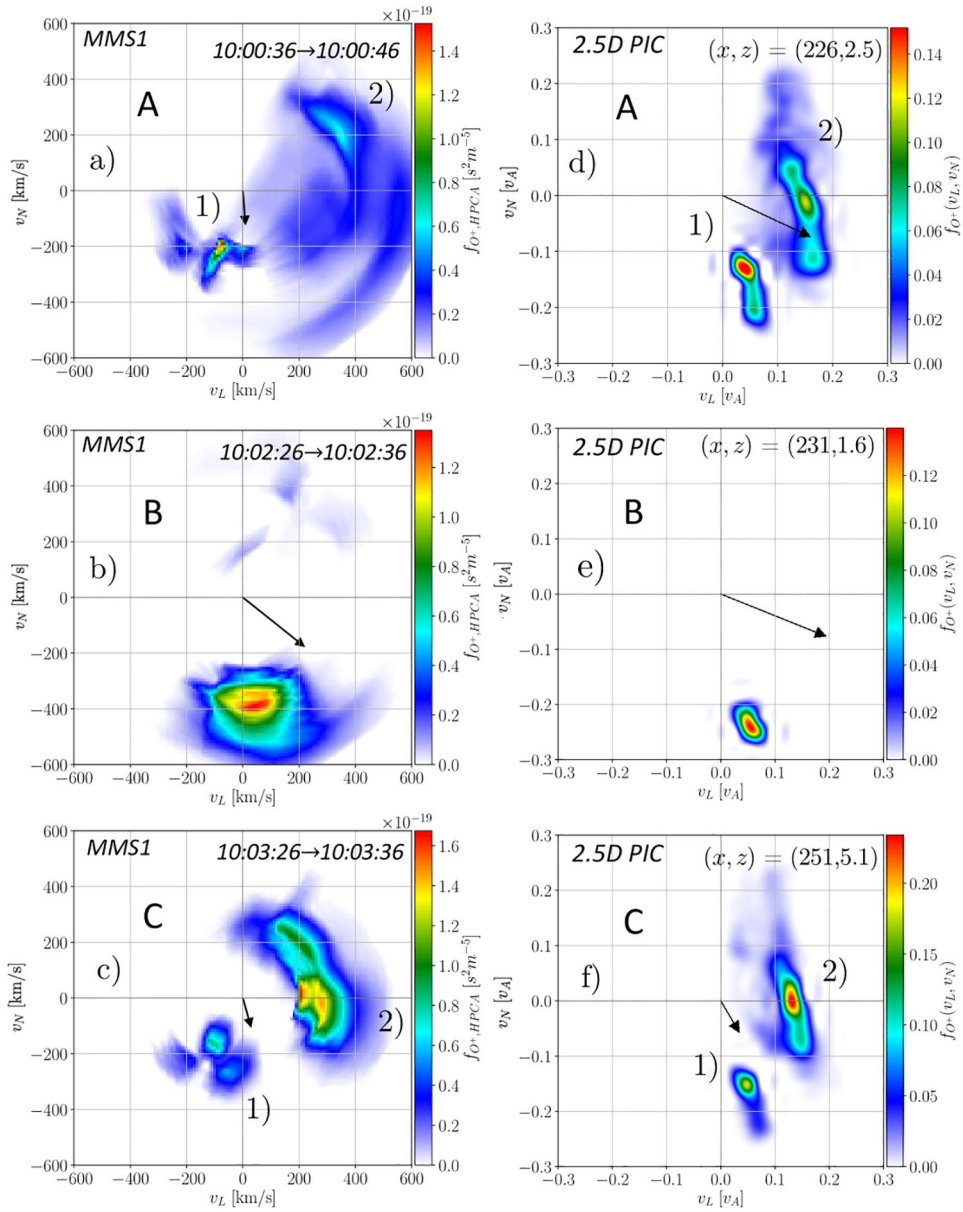

Figure 3. O^+ VDFs $f_{O^+}(v_L, v_N)$ at three locations marked A, B, and C in Figure 1. (a–c) HPCA. (d–f) PIC. The arrows represent $v_{E\times B}$ which, for the observations, are time-averaged over the collection time of the distribution. The normalization speed from observations (v_A = 920 km/s) shows good agreement in speeds between $f_{O+}^{HPCA}(v_L, v_N)$ and $f_{O+}^{PIC}(v_L, v_N)$, with the simulation being slightly lower.

4.2. O^+ Distribution Function Comparison

In Figure 1, the extracted fields, and velocity and density moments along the spacecraft trajectory correspond well to those observed by MMS. To investigate if the velocity space signatures in the vicinity of the density cavity also agree between simulations and observations, we extract the VDFs at locations A, B, and C (marked in Figure 1).

In Figure 3, we see the side-by-side comparison of the HPCA (Figures 3a–3c) and PIC (Figures 3d–3f) O^+ VDFs, defined as $f_{O^+}(v_L, v_N) = \int f_{O^+}(v_L, v_M, v_N) dv_M$. The $v_{E\times B}$-components are shown as the black arrow in all panels. At A, both $f_{O+}^{HPCA}(v_L, v_N)$ and $f_{O+}^{PIC}(v_L, v_N)$ are dominated by two distinct populations; (1) a colder population with $v_N < 0$, and (2), a warmer population spanning both positive and negative v_N. These two populations are well separated in v_L. The colder population is formed as O^+, originating from the northern

inflow region, is accelerated by E_N, resulting in the ion passing straight through the upward expanding density enhancement and continuing its motion toward the neutral line. Population 2 exhibits a large spread in $v_N^{O^+}$ and primarily consist of particles originating from the south. The part of the population displaying $v_N < 0$ have been reflected by the Lorentz force $- v_N^{O^+} B_L$ and subsequently $v_M^{O^+} B_L$ to obtain a negative $v_N^{O^+}$. The positive $v_N^{O^+}$ part consists of particles that have not yet undergone a reflection. The obtained $v_L^{O^+}$ is produced by the Lorentz forces $- v_N^{O^+} B_M$ and $v_M^{O^+} B_N$. The Lorentz force $- v_N^{O^+} B_M$ is a result of the E_N-accelerated oxygen ions encountering the Hall magnetic field B_M whereas the $v_M^{O^+} B_N$ is due to the encounter of B_N after acceleration by the reconnection electric field E_M. Thus, part of $v_N^{O^+}$ and $v_M^{O^+}$ is diverted into $v_L^{O^+}$. The difference in $v_L^{O^+}$ between populations 1 and 2 is attributed to the time spent in the exhaust. The oxygen ions constituting population 1 enters from the northern lobe and thus the time spent in the exhaust is considerably less than that of the southern lobe originating particles in population 2 (recall that the VDFs are extracted on the northern side of the current sheet). Diversion from $v_M^{O^+}$ to $v_L^{O^+}$ for population 2 occurs over a greater time compared to population 1, resulting in a significantly stronger $v_L^{O^+}$. For population 2, we observe a slight increase of $v_L^{O^+}$ for decreasing $v_N^{O^+}$ velocities. After reflection, particles with large negative $v_N^{O^+}$ have experienced an acceleration by E_M due to the long time spent in the exhaust. During this time, an increase in v_L is realized by the Lorentz force $v_M^{O^+} B_N$. We further note that $v_L^{O^+}$ is dependent on where the oxygen ions enters within the exhaust.

In Figure 3b, we compare the VDFs at location B which is within the region of strong v_N-flows. Despite the low density for the observations, the count is considered sufficient to calculate a credible VDF at this location in the cavity. The beam at location B consists of O^+ that have a strong negative v_N centered around – 400 km/s and it matches well the corresponding behavior seen in the simulation (Figure 3e). The O^+ from simulation obtains such a v_N through ballistic acceleration by E_N. Further, the simulation reveals that this population moves to form the oxygen wavefront. The demagnetized behavior of the O^+ seen in Figure 2, along with the strong agreement of the VDFs, leads us to conclude that the mechanism to produce the O^+ dynamics in the observations is similar to the simulation.

The VDF captured at the second encounter of the density edge (C) is seen in Figure 3c. The exceptional similarities of the signatures in the VDFs at the location of the density enhancements at location A and C indicates that these two enhancements are either of the same nature or created by similar mechanisms.

A difference between the VDFs provided by MMS and the ones seen in the PIC simulation is that of the $v_L^{O^+}$. In Figures 3a and 3c, we see that populations 1 and 2 exhibit different signs of $v_L^{O^+}$, while in the simulation, both populations display $v_L^{O^+} > 0$. Furthermore, at B, the Hall accelerated $v_N^{O^+}$ from PIC (Figure 3e) display a clear $v_L^{O^+}$ whereas the observational population (Figure 3b) appears to be centered closer to $v_L^{O^+} = 0$ km/s. This feature is attributed to the tailward streaming nature of the oxygen during the event and is not accounted for in the simulation—which considers the O^+ to be at rest. Regardless, the overall features and distribution of the particles match that of the simulation impressively well.

In Figure 4, we see $v_L^{O^+}$ together with **B**. Prior to the encounter of the reconnection region at ~10:00 UT, HPCA measures stable flows of tailward streaming O^+ reaching bulk velocities of $v_L^{O^+} \approx -180$ km/s. Previous studies have shown that the momentum of oxygen ions can induce a motion of the reconnection site regardless of its degree of magnetization (Kolstø et al., 2020b). In our case, due to the relatively low oxygen density, the effect on the center-of-mass velocity is low $v_{COM} \approx -19$ km/s. Hence, we expect the X-line motion induced by the oxygen flow to be low. However, the initial motion of the ions can be superposed with the motion gained during the reconnection process, which in our case would account for the differences in $v_L^{O^+}$ between simulations and observations. The average tailward flow of O^+ prior to the reconnection site (between 09:41 and 09:57) is found to be $v_{LOBE}^{O^+} \approx -110$km/s. A shift in the L-direction of $v_{LOBE}^{O^+}$ resolves the sign disparities of $v_L^{O^+}$ between HPCA and the simulation. Although the tailward flow of the oxygen ions decreases toward the reconnection site entrance (~10:00 UT), this can be due to local variations, and the added v_L velocities may be due to such variations that are present within the exhaust.

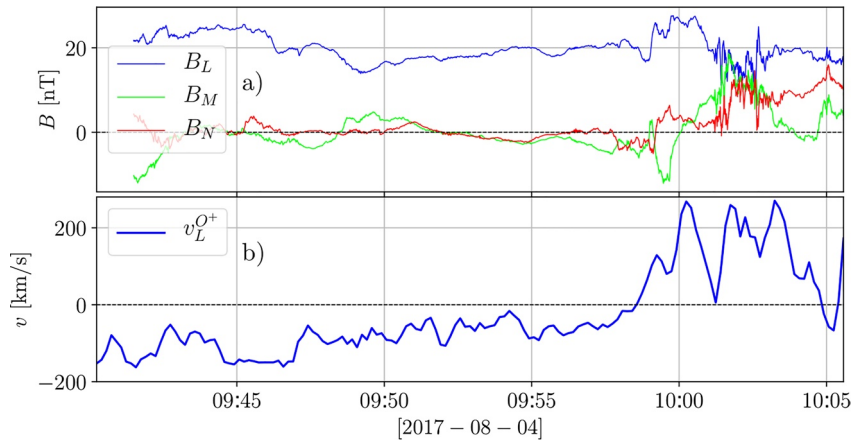

Figure 4. (a) Magnetic field, and (b) L-directed velocity of O^+ prior to the encounter of the reconnection region showing clear signs of tailward streaming oxygen ions.

4.3. Expanding Oxygen Wave

In this section, we discuss how the different populations seen in the VDFs in Figure 3 are expected signatures to be found in the vicinity of an oxygen wave. Inside the O^+ density cavity (location B), MMS observes cold lobe ions that are captured by the Hall electric field, and have started to move toward the current sheet (Figure 3b). Adjacent to the cavity (locations A and C), MMS still observe the cold lobe plasma accelerated toward the current center by E_N (population 1 in Figures 3a and 3c). In addition to the cold population, MMS observes a hot O^+ jet (population 2) that has likely undergone a significant acceleration by the reconnection electric field. This hotter population is the population that predominantly contributes to the bulk reconnection outflow. Locations A and C can therefore be considered as part of the reconnection outflow. In contrast, B is located where the outflow is still not present, i.e., downstream of the reconnection oxygen jet front. We, therefore, suggest that the transition from A or C to B is a signature of an expanding oxygen wave.

5. Discussion and Summary

In this paper, we have investigated the behavior of oxygen ions in the reconnection exhaust. The clear reconnection signatures captured by MMS, in the presence of O^+, enabled us to study the dynamics of the oxygen ions in great detail. To provide context to these observations, we utilized a 2.5D PIC simulation to construct a simple, time-evolutionary, trajectory to search for a probable path of MMS1 with respect to the reconnection region. The remarkable match of **E**, **B**, as well as the bulk and density moments between the simulation and observations provides a confident contextualization of the MMS data. Along the inferred MMS trajectory, we extracted O^+ VDFs at locations A, B, and C which further displayed a strong agreement between HPCA and PIC.

Based on the O^+ density structures encountered by MMS, and the signatures of the VDFs, we hypothesized that the spacecraft passed the same density ridge twice; (1) At the entrance of the exhaust (A), and (2) at the exit (C) after an expansion of the O^+ striation (occurring over a time of $\sim 325\Omega_p^{-1}$). The crossings through locations A and C marks the encounter of the oxygen wave, which is further supported by the observed density cavity at location B. Such density cavities are expected to be found as these regions represent the low-density wake after the collective E_N acceleration of O^+ giving rise to the oxygen wave (Tenfjord et al., 2018; Kolstø et al., 2020a). We acknowledge that there is a discrepancy between points A and C concerning the time covered by the spacecraft and the scaled simulation time and that this might be due to the structure evolving at different rates, exhibiting different spatial scales, or being structurally different. Further, the simulation is based on cold O^+ at rest in the inflow region, while in the current event the O^+ have a finite bulk velocity and temperature, which may conspire to alter the structure scale and evolution compared to the simulation.

The results reported in this study provide insight into the O^+ dynamics in the reconnection exhaust. Our comparison of MMS data with PIC modeling shows a remarkable agreement. This match suggests strongly that the features in the observations are, in fact, signatures of an oxygen wave.

Data Availability Statement

The simulation data set used is available at Kolstø (2021). MMS data are available online at MMS Science Data Center (2020).

Acknowledgments
This study was supported by the University of Bergen, by NOTUR/NORSTOR under Project NN9496 , and by NASA's MMS mission. Cecilia Norgren and Paul Tenfjord received support from the Research Council of Norway under Contract 30086. Further, we acknowledge the SPEDAS and pySPEDAS analysis tools.

References

Baker, D. N., Hones, E. W., Young, D. T., & Birn, J. (1982). The possible role of ionospheric oxygen in the initiation and development of plasma sheet instabilities. *Geophysical Research Letters*, *9*(12), 1337–1340. https://doi.org/10.1029/GL009i012p01337

Chappell, C. R., Moore, T. E., & Waite, J. H. (1987). The ionosphere as a fully adequate source of plasma for the Earth's magnetosphere. *Journal of Geophysical Research*, *92*(A6), 5896–5910. https://doi.org/10.1029/JA092iA06p05896

Ergun, R. E., Tucker, S., Westfall, J., Goodrich, K. A., Malaspina, D. M., Summers, D., et al. (2016). The axial double probe and fields signal processing for the MMS mission. *Space Science Reviews*, *199*(1), 167–188. https://doi.org/10.1007/s11214-014-0115-x

Frank, L. A., Ackerson, K. L., & Yeager, D. M. (2012). Observations of atomic oxygen (O+) in the Earth's magnetotail. *Journal of Geophysical Research*, *82*(1), 129–134. https://doi.org/10.1029/JA082i001p00129

Grande, M., Perry, C. H., Hall, A., Fennell, J., Nakamura, R., & Kamide, Y. (2013). *What is the effect of substorms on the ring current ion population during a geomagnetic storm?* (pp. 75–89). American Geophysical Union (AGU). https://doi.org/10.1029/142GM08

Hesse, M., Schindler, K., Birn, J., & Kuznetsova, M. (1999). The diffusion region in collisionless magnetic reconnection. *Physics of Plasmas*, *6*(5), 1781–1795. https://doi.org/10.1063/1.873436

Kistler, L. M., Mouikis, C., Möbius, E., Klecker, B., Sauvaud, J. A., Réme, H., & Balogh, A. (2005). Contribution of nonadiabatic ions to the cross-tail current in an O+ dominated thin current sheet. *Journal of Geophysical Research*, *110*, A06213. https://doi.org/10.1029/2004JA010653

Kolstø, H. M. (2021). *Replication data for: MMS observations of an expanding oxygen wave in magnetic reconnection*. DataverseNO. https://doi.org/10.18710/0PBOGL

Kolstø, H. M., Hesse, M., Norgren, C., Tenfjord, P., Spinnangr, S. F., & Kwagala, N. (2020a). Collisionless magnetic reconnection in an asymmetric oxygen density configuration. *Geophysical Research Letters*, *47*, e2019GL085359. https://doi.org/10.1029/2019GL085359

Kolstø, H. M., Hesse, M., Norgren, C., Tenfjord, P., Spinnangr, S. F., & Kwagala, N. (2020b). On the impact of a streaming oxygen population on collisionless magnetic reconnection. *Geophysical Research Letters*, *47*, e2020GL089462. https://doi.org/10.1029/2020GL089462

Liang, H., Lapenta, G., Walker, R. J., Schriver, D., El-Alaoui, M., & Berchem, J. (2017). Oxygen acceleration in magnetotail reconnection. *Journal of Geophysical Research: Space Physics*, *122*, 618–639. https://doi.org/10.1002/2016JA023060

Lindqvist, P.-A., Olsson, G., Torbert, R. B., King, B., Granoff, M., Rau, D., et al. (2016). The spin-plane double probe electric field instrument for MMS. *Space Science Reviews*, *199*(1), 137–165. https://doi.org/10.1007/s11214-014-0116-9

Liu, Y. H., Kistler, L. M., Mouikis, C. G., Roytershteyn, V., & Karimabadi, H. (2014). The scale of the magnetotail reconnecting current sheet in the presence of O+. *Geophysical Research Letters*, *41*, 4819–4827. https://doi.org/10.1002/2014GL060440

Liu, Y. H., Mouikis, C. G., Kistler, L. M., Wang, S., Roytershteyn, V., & Karimabadi, H. (2015). The heavy ion diffusion region in magnetic reconnection in the Earth's magnetotail. *Journal of Geophysical Research: Space Physics*, *120*, 3535–3551. https://doi.org/10.1002/2015JA020982

MMS Science Data Center. (2020). Retrieved from https://lasp.colorado.edu/mms/sdc/public/

Moore, T. E., Chandler, M. O., Fok, M.-C., Giles, B. L., Delcourt, D. C., Horwitz, J. L., & Pollock, C. J. (2001). Ring currents and internal plasma sources. *Space Science Reviews*, *95*(1–2), 555–568. https://doi.org/10.1023/A:1005264907107

Mouikis, C. G., Kistler, L. M., Liu, Y. H., Klecker, B., Korth, A., & Dandouras, I. (2018). H+ and O+ content of the plasma sheet at 15–19 Re as a function of geomagnetic and solar activity. *Journal of Geophysical Research: Space Physics*, *115*, A00J16. https://doi.org/10.1029/2010JA015978

Pollock, C., Moore, T., Jacques, A., Burch, J., Gliese, U., Saito, Y., et al. (2016). Fast plasma investigation for magnetospheric multiscale. *Space Science Reviews*, *199*(1), 331–406. https://doi.org/10.1007/s11214-016-0245-4

Russell, C. T., Anderson, B. J., Baumjohann, W., Bromund, K. R., Dearborn, D., Fischer, D., et al. (2016). The magnetospheric multiscale magnetometers. *Space Science Reviews*, *199*(1), 189–256. https://doi.org/10.1007/s11214-014-0057-3

Shay, M. A., & Swisdak, M. (2004). Three-species collisionless reconnection: Effect O^+ of on magnetotail reconnection. *Physical Review Letters*, *93*(17), 175001. https://doi.org/10.1103/PhysRevLett.93.175001

Sonnerup, B. U. Ö., & Cahill, L. J. (1967). Magnetopause structure and attitude from Explorer 12 observations. *Journal of Geophysical Research*, *72*(1), 171–183. https://doi.org/10.1029/JZ072i001p00171

Tenfjord, P., Hesse, M., & Norgren, C. (2018). The formation of an oxygen wave by magnetic reconnection. *Journal of Geophysical Research: Space Physics*, *123*, 9370–9380. https://doi.org/10.1029/2018JA026026

Tenfjord, P., Hesse, M., Norgren, C., Spinnangr, S. F., & Kolstø, H. (2019). The impact of oxygen on the reconnection rate. *Geophysical Research Letters*, *46*, 6195–6203. https://doi.org/10.1029/2019GL082175

Toledo-Redondo, S., André, M., Aunai, N., Chappell, C. R., Dargent, J., Fuselier, S. A., et al. (2021). Impacts of ionospheric ions on magnetic reconnection and Earth's magnetosphere dynamics. *Reviews of Geophysics*, *59*, e2020RG000707. https://doi.org/10.1029/2020RG000707

Wilken, B., Zong, Q. G., Daglis, I. A., Doke, T., Livi, S., Maezawa, K., et al. (1995). Tailward flowing energetic oxygen ion bursts associated with multiple flux ropes in the distant magnetotail: GEOTAil observations. *Geophysical Research Letters*, *22*(23), 3267–3270. https://doi.org/10.1029/95GL02980

Wygant, J. R., Cattell, C. A., Lysak, R., Song, Y., Dombeck, J., McFadden, J., et al. (2005). Cluster observations of an intense normal component of the electric field at a thin reconnecting current sheet in the tail and its role in the shock-like acceleration of the ion fluid into the separatrix region. *Journal of Geophysical Research*, *110*, A09206. https://doi.org/10.1029/2004JA010708

Young, D. T., Burch, J. L., Gomez, R. G., De Los Santos, A., Miller, G. P., Wilson, P., et al. (2016). Hot plasma composition analyzer for the magnetospheric multiscale mission. *Space Science Reviews*, *199*(1), 407–470. https://doi.org/10.1007/s11214-014-0119-6

Zong, Q.-G., Wilken, B., Woch, J., Mukai, T., Yamamoto, T., Reeves, G. D., et al. (1998). Energetic oxygen ion bursts in the distant magnetotail as a product of intense substorms: Three case studies. *Journal of Geophysical Research*, *103*(A9), 20339–20363. https://doi.org/10.1029/97JA01146